45th European Rotorcraft Forum
Warsaw, Poland, 17-20 September,
2019
Paper 41

TOWARDS OPTIMISATION OF COMPOUND ROTORCRAFT

Tao Zhang [1] and George N. Barakos [2]
CFD Laboratory, School of Engineering, University of Glasgow, G12 8QQ, U.K.
www.gla.ac.uk/cfd

Abstract

This work presents a tool-chain development for aerodynamic analysis and optimisation of compound rotorcraft. An automation framework for geometry composition and grid generation using ICEM Hexa is proposed, and variable applications are presented. High-fidelity CFD simulations of ducted fans are first performed to validate the in-house solver HMB3. Detailed analyses of the ducted fan and comparisons against experiments and simpler methods are presented, and good correlation can be noted. A compound helicopter model is then assembled, consisting of a parametrised Dauphin-like fuselage, ducted fans for auxiliary thrust, and a main rotor. Simulation methods of several fidelity levels using steady/unsteady actuator disks and resolved blades are conducted and evaluated. Analyses of the aerodynamics and flow features are then presented.

1 INTRODUCTION

Compound rotorcraft is a generalisation of the term compound helicopters proposed by Graham[1]:"a rotorcraft which, in flight, and at slow speed derives the substantial proportion of its lift from a rotary wing system but at speed can generate lifting and longitudinal thrust from a suitable combination of rotary wing system, fixed lifting surface(s) and auxiliary propulsor(s)".

A rotorcraft of this type possesses, simultaneously, the high-speed performance of a fixed-wing plane and the hover efficiency of a conventional helicopter, and is ideal for use as emergency/medical evacuation or urban taxi operations. For conventional helicopters, through compounding, the inherent speed limitations can be effectively overcome. The result is superior performance e.g. high payload/lift capacity, lower fuel burn, and increased range and speed. Their increased capabilities allow compound rotorcraft to bridge the gap between traditional helicopters and fixed-wing aircraft, and fill the mission gap between airplanes and conventional low-speed helicopters[2].

However, the combination of multiple sources of lift and thrust brings significant challenges in terms of aerodynamic interactions, vibration and stability, control and trim, power allocation *etc.*Furthermore, less data and few research works are published comparing to conventional helicopters, and significant research and developments need to be carried out. Methods like CFD are frequently used, but to reach the necessary efficiency, several modelling options must be studied. A tool-chain accounting for shape parametrisation and grid generation is also necessary for analysis and optimisation studies.

In the present work, an automation framework for geometry composition and grid generation using ICEM Hexa for mesh generation and an in-house CFD solver is proposed. The framework is enabled to accommodate large geometry variations. To validate the HMB3 methods[3], a ducted fan test case by NASA[4] is used. Since very few data is given in the report, comparisons are also made against the method of Drela[5][6]. Detailed comparisons and performance analyses are presented. A compound helicopter model is then assembled, consisting of a parametrised Dauphin-like fuselage, ducted fans for auxiliary thrust, and a main rotor. Resolving the rotor and propeller blades involved will certainly require large scale CFD computing. Nevertheless, to study the interactions between rotor wake/fuselage/ducted fan, an unsteady actuator line method is also used. The method is capable of modelling the complex rotor wake structure with efficiency.

[1]PhD Student - 2354711Z@student.gla.ac.uk
[2]Professor - george.barakos@glasgow.ac.uk - corresponding author

2 AUTOMATIC GRID GENERATION FRAMEWORK

As a key part of CFD analyses and optimisation, mesh generation demands a significant amount of efforts and human interaction. An automation framework for geometry composition and grid generation is therefore proposed in the present work using the ICEM Hexa mesher. This framework is capable of delivering geometry models for CAD tools and ready-to-run, multi-block, structured grids for CFD solvers from a given set of parameters.

A schematic of the current framework is presented in Figure 1. The framework is implemented using in-house codes, ICEM Hexa scripts, and Unix shell scripts. Through in-house pre-processing codes, the input geometry is analysed and parametrised. Definitive features, e.g. sectional profiles, are extracted and exported using ICEM-compatible formats. Parameters governing the geometry generation as well as the meshing process, e.g. outer boundary distance, first layer height of the boundary layer mesh, boundary layer cell numbers, are defined and translated into script parameters.

With these parameters defined, prescribed scripts for different shape patterns, e.g. blade/wing, fuselage, or duct, are then executed by ICEM. Modules of the ICEM scripts are presented in Figure 2. The blocking process, a major part of the mesh generation that needs extensive human interaction, is realised by importing pre-defined topologies (blocking files) and re-associating the projection. The design of these topologies for specific shape patterns, however, still needs human intervention in the interest of fine mesh quality.

NURBS based geometries and multi-block structured grids will be generated and exported. The post-processing codes convert the output to CFD solvers and external CAD tools. With a high degree of automation and versatility, this framework can be incorporated into various gradient- or meta-model-based optimisation cycles.

Applications for variable blade shapes are presented in Figures 3(a), 3(b), and 3(c). The framework has shown good flexibility and versatility for variations e.g. aspect ratio, twist distribution, swept/anhedral. The framework is also tested using distinct duct shapes with the thick NACA0050 profile (Figure 4(a)) and the highly cambered, thin NACA8406 4(b) profile. The grids can afterwards be assembled using Chimera methods from a correct set of transformational parameters as shown in Figures 5(a) and 5(b).

3 COMPUTATIONAL METHODS

The Helicopter Multi-Block (HMB3) [7, 8] code is used in the present work. HMB3 solves the Unsteady Reynolds Averaged Navier-Stokes (URANS) equations in integral form using the Arbitrary Lagrangian Eulerian (ALE) formulation for time-dependent domains, which may include moving boundaries. Chimera/overlapping grids methods are implemented to allow for complex relative motions of various parts. The Navier-Stokes equations are discretised using a cell-centred finite volume approach on a multi-block grid. The spatial discretisation of these equations leads to a set of ordinary differential equations in the temporal domain.

$$\frac{d}{dt}\left(\mathbf{W}_{i,j,k}V_{i,j,k}\right) = -\mathbf{R}_{i,j,k}\left(\mathbf{W}_{i,j,k}\right), \tag{1}$$

where i,j,k represent the cell index, $\mathbf{W}$ and $\mathbf{R}$ are the vector of conservative flow variables and flux residual respectively, and $V_{i,j,k}$ is the volume of the cell i,j,k. To evaluate the convective fluxes Osher [9] approximate Riemman solver is used, while the viscous terms are discretised using a second order central differencing spatial discretisation. The Monotone Upstream-centered Schemes for Conservation Laws (MUSCL) approach developed by Leer [10] is used to provide high-order accuracy in space. The HMB3 solver uses the alternative form of the Albada limiter [11] being activated in regions where large gradients are encountered, mainly due to shock waves, avoiding the non-physical spurious oscillations. An implicit dual-time stepping method is employed to perform the temporal integration, where the solution is marching in pseudo-time iterations to achieve a fast convergence, which is solved using a first-order backward difference. The linearised system of equations is solved using the Generalised Conjugate Gradient method with a Block Incomplete Lower-Upper (BILU) factorisation as a preconditioner [12]. To allow for easy sharing of the calculation load for a parallel job, multi-block structured grids are used. Various turbulence models are available in the HMB3 solver, including several one-equation, two-, three- and four-equation turbulence models. Furthermore, Large-Eddy simulation (LES), Detached-Eddy Simulation (DES), and Delayed-Detached-Eddy Simulation (DDES) are also available. In the present work the baseline k-ω [13], $k-\omega$ SST [13] turbulence models are used.

3.1 Actuator Disk Models

The actuator disk model represents the rotor effects by simply introducing a pressure jump across an infinitesimally thin disk. The implementation in HMB3 only requires the addition of sources terms in the momentum and the energy equations. Flow features around the blades are not resolved in detail and limited additional computational cost is needed. Several actuator disk models are implemented in HMB3[14], and the details are presented herein.

Steady Uniform/Nonuniform Actuator Disk

For a uniform actuator disk, which assumes even thrust distribution over the disk, the pressure jump across the disk can be expressed as the non-dimensional form below:

$$\Delta P = \frac{T}{\rho_\infty V_\infty^2 A} = \frac{C_T}{2\mu^2}. \tag{2}$$

The pressure jump can be implemented by additional source terms in the momentum and energy equations. Nonetheless, more delicate pressure distribution can be imposed to imitate the nonuniform pressure distribution in forward flight. The nonuniform actuator disk model proposed is adopted and implemented in HMB3. The pressure jump distribution over the disk is expressed as:

$$\Delta P = \rho_\infty \gamma \big[\frac{\gamma sign(\delta)}{2} + V_\infty cos(\alpha_\infty - \alpha + \delta)\big], \tag{3}$$

where δ is the angle of the vortex cylinder slope, $(\alpha_\infty - \alpha)$ denotes the actual incidence of the rotor inflow. γ is the circulation distribution on the disk, which is a function of the radial position and the azimuth:

$$\gamma = k_1 r^2 (2 - r^2 - r^4) + k_2 \mu_i \gamma_0 \big(\frac{1}{r} - \frac{25}{13} r\big) sin(\Psi), \tag{4}$$

where μ_i is the advance ratio calculated by free-stream can induced speeds. k_1 and k_2 are empirical coefficients that can be calibrated through experimental data. Approximations of these coefficients can be defined as:

$$\begin{cases} k_1 = 1.989 V_\infty \Big[- cos(\alpha_\infty - \alpha + \delta) \\ \quad + \sqrt{cos^2(\alpha_\infty - \alpha + \delta) + 1.27 \dfrac{C_T}{\mu^2}} \Big], \\ k_2 = \dfrac{8\mu_i \left[1 + tan^2(\delta^*)\right] + a\sigma tan(\delta_*)}{\left[1 + tan^2(\delta^*)\right] \left[4\mu_i + a\sigma tan(\delta^*)\right]}, \end{cases} \tag{5}$$

where $\delta^* = \big(\frac{\pi}{4} - \frac{|\delta|}{2}\big)$, a is the slope of the lift coefficient, and σ is the rotor solidity.

Unsteady Actuator Disk

To resolve more details of the rotor wake, including the rotation of blades, the unsteady actuator disk model is introduced and implemented in HMB3. The idea is to imitate the blades and their motion with actuator lines. The load distribution is re-shaped with regard to the actuator lines using a Gaussian function η:

$$\eta = \sum_{j=1}^{N_b} exp\big(- \frac{|S_j|^2}{\epsilon^2}\big), \tag{6}$$

where N_b is the number of blades, ϵ is the mean aerodynamic chord of the blade, and $|Sj|$ is the arc between the cell centre and the actuator line. The source term can thus be written as:

$$f = \sum_{i=1}^{N} \Big(\frac{A_i \Delta P}{\sqrt{\pi}\sigma} \eta_i |A| \Big), \tag{7}$$

where N is the number of cells representing the actuator disk, A_i is the area of the cell, ΔP is the pressure jump through momentum theory, and σ is the solidity of the blade. Whereas $|A|$ is a normalising factor to ensure the overall thrust by the disk is equivalent to the steady actuator disk counterpart. $|A|$ can be given as:

$$|A| = \frac{A}{\sum_{i=1}^{N} (\eta_i A_i)}. \tag{8}$$

4 DUCTED FAN VALIDATION

To validate the HMB3 CFD solver [3] for ducted fans, a case by NASA [4] is used. Test conditions for this case are presented in Table 1. The ducted fan is operating at the maximum wind speed of $100 ft/s$ with a constant rotational speed of $8,000 RPM$, which was the highest advance ratio case of the experiments. The Reynolds number based on the free-stream speed, and the duct chord length is around $550,000$. It should be noted that the blade pitch angle at 70% span is set as $29.58°$, instead of the $24°$ in the report [4]. This value is obtained through matching the overall thrust of the ducted fan using DFDC (Ducted Fan Design Code) by Drela *et al.* [5][6].

The empty duct without the propeller and the open propeller configuration are also simulated and presented for comparisons. Since very few data are given in the report, comparisons are also made against the methods of Drela [5][6][15].

The geometry and the employed coordinate system are presented in Figure 6(b). The rear part of the centre-body is sealed with a smooth shape, whereas in the experiments it was attached to the wind tunnel support structures. To allow for the relative motion of blades and to simplify the mesh generation, Chimera methods are adopted. As shown in Figure 6(b), a multi-block, structured grid for the duct and the centre-body is used as the background grid, where separate grids for blades are generated. It should be noted that the tip and root clearance is preserved in accordance with the experiments in current simulations, as the tip leakage flow may have a significant impact on the performance.

4.1 Comparisons and Validation

Drag polar comparisons for the empty duct cases are presented in Figure 7. Good agreement with experimental data can be noted until high angles of attack. The discrepancy there is due to the separation at the outer surface of the duct, which can hardly be resolved accurately by the steady simulation applied.

Comparisons for the complete ducted fan configuration between the experimental data and the HMB3 simulation, as well as the breakdown of propulsion forces, are listed in Table 2, and good agreement can be noticed between CFD, simpler predictive methods [15][5][6] as well as the test data. For the convenience of comparing, all force and moment data are normalised using the far-field dynamic pressure, the duct chord length C_{df}, and the projected duct area S_{df}.

Results using the DFDC code [5][6] are obtained by matching the overall thrust. This results in a $\theta_{0.7}$ of 29.58° under the same RPM, far-field speed and geometries. The same pitch setting is also applied in the CFD simulations. Figures 8(a) and 8(b) show good correlation between the methods for averaged pressure distributions along the centre-body and duct. Relative differences with respect to the experimental results are presented in Table 3. It can be noted that differences between the HMB3 results and the experiments are minor.

4.2 Performance Analysis

Further performance analyses and comparisons are also made against the open-propeller configuration and the static duct. Since no open propeller tests were conducted during experiments [4], comparisons are made against XROTOR [15] calculations as presented in Table 2. Aerodynamic loads from the HMB3 and XROTOR codes are in good agreement with a difference of 2.6% for axial (propulsive) forces.

It can be clearly seen from Figures 9(a) and 9(b) that the presence of the duct significantly suppressed the strength of tip vortices. Further, as shown in Figures 10(a) and 10(b), the inflow is accelerated by the duct curvature at the inlet, leading to the lower regional static pressure. This causes the blades to work at higher inflow velocities. The axial mass and momentum flow rates measured at the diffuser exit for all configurations are presented in Table 4. As can be noted, the presence of the duct increases both the mass and the momentum flow rates, as agreed by simple momentum theory. The diffuser forces the flow to expand, thereby slowing down the axial speed and recovering the static pressure. The conversion of the dynamic and the static pressures are presented in Figures 12(a) and 12(b).

To further verify the contribution of the duct, the pressure coefficient distribution and surface pressure vectors are presented in Figure 11. It is clearly shown that the leading edge suction, and the higher pressure at the diffuser together contributed the main percentage of the thrust gain. The propeller significantly decreases the pressure on the inner side of the duct, especially at the leading-edge before the rotor disk, where the suction happens. A pressure jump is caused by the rotor disk. A low pressure peak limited to a very small area can be observed due to the sudden transition of the geometry at the diffuser. The static pressure is then gradually recovered by the diffuser. Slightly higher static pressure on the outer surface from the leading-edge to the mid-span is also resulted.

The performance of the ducted fan blades and the open propeller blades are also analysed and compared. Radial distribution of the aerodynamic loads are present in Figures 13(a) to 13(b). It can be noted in the figures, as well as in Table 2 that the ducted fan propeller, produces less thrust in comparison to the open propeller. This can be attributed to the lager induced inflow velocity by the duct as mentioned earlier. The overall thrust of the ducted fan, taking into account of the duct, however, is higher than the open propeller. It is also shown that the tip loss of the ducted fan propeller is restricted, resulting in an almost linear thrust distribution.

It can also be noted that the torque produced by the open propeller is higher due to the larger induced drag. As shown in Table 5, torque contributions from the duct and the centre-body are minor. Nevertheless, the overall thrust of the ducted fan is higher, indicating the superior efficiency of ducted fans as presented in Table 2. Although the performance improvement is moderate due to the high advance ratio in this case.

5 SIMULATIONS OF COMPOUND ROTORCRAFT

In the present work, a compound helicopter model is assembled, consisting of a parameterised Dauphin-like fuselage, ducted fans for auxiliary thrust, and a main rotor. Resolving the rotor and propeller blades involved will certainly require large scale CFD computing. Nevertheless, to study the interactions between rotor wake/fuselage/ducted fan with efficiency, actuator disk models described in Section 3.1 are utilised. Blade representations of three fidelity levels, *i.e.* the steady nonuniform actuator disk, the unsteady actuator line, and the resolved blades, are considered and evaluated. Test conditions for the simulations are listed in Table 6.

Figures 14(a), 14(b), and 14(c) show the mesh topology with actuator disk models and resolved blades. Multi-block, structured grids are generated separately for the ducts, the fuselage, and the blades. Grids are assembled using Chimera methods, ensuring the flexibility of modifying positions of the components.

Figures 15(a), 15(b), and 15(c) show the wake structure at a low advance ratio obtained using the three methods mentioned earlier. Due to the coarse blade grids employed, the wake is not well resolved in Figure 15(c), but the structure of the blade tip and root vortices can still be observed. The steady actuator disk offers an averaged wake structure and no flow details due to the blades can be observed. The unsteady actuator line model, however, resolved not only the separate tip vortices, but also a few details of the root vortices and the superstructures of the far wake. Figure 16 shows more details of the flow features using unsteady actuator lines with refined grids for wake capture. Interactions

between the rotor wake and the ducted fan wake can be observed. As shown in Figure 16, the method is capable of modelling the complex rotor wake structure with efficiency.

Lift force variations and the averaged values on the fuselage, obtained through different rotor representations, are shown in Figure 17. As can be noted, steady actuator disks and unsteady actuator lines give the same averaged loads. Fluctuations imposed by the unsteady actuator lines are in good correlation with resolved blade results, while the efficiency of the unsteady actuator line should be emphasised.

To further study influence of the main rotor on the ducted fans, inflow angles, measured as angles between the flow velocity and the axial direction at the slice $0.125c_{df}$ ahead the duct leading edge, are presented in Figures 18(a) to 18(c). As can be seen, most inflow distortion is induced by the duct leading edge curvature. However, effects of the main rotor downwash, especially at the advancing side, can be noticed, which leads to the asymmetry of the angle distribution. All three blade representations are able to resolve such asymmetry, whereas the resolved blades offer solutions with more detailed blade loads and wake.

6 CONCLUSIONS

An automation framework for geometry composition and grid generation has been implemented pertinent to compound rotorcraft. High-fidelity simulations of a ducted fan test case are performed and analysed. Simulations and analyses of a compound helicopter model are also presented. From the presented work, the following conclusions can be drawn:

1. The proposed automation framework has shown great flexibility and versatility for large shape variations. With a high degree of automation, the framework can be further evaluated and incorporated into optimisation circulations.

2. For the ducted fan simulation, good correlation between the HMB3 methods, experiments, and lower-order methods can be noticed. At the test conditions, the ducted fan is shown to have superior performance over its open propeller counter part. The duct is shown to be the major source of the thrust gain, due to the leading-edge suction and the higher static pressure at the diffuser exit. The ducted fan blades produce less thrust than the open propeller counter part due to the higher inflow velocities, but the torque generated is also decreased. Overall, the ducted fan can be an ideal choice of propulsion for future compound rotorcraft and needs to be further studied.

3. HMB3 demonstrated its capability and flexibility for simulations of compound rotorcraft with multiple components. Methods of various fidelity levels using steady/unsteady actuator disks and resolved blades are put forward and compared, while the efficiency and the effectiveness of the unsteady actuator disk should be emphasised.

7 ACKNOWLEDGEMENT

The sponsorship of the University of Glasgow and the China Scholarship Council is gratefully acknowledged.

8 REFERENCES

References

[1] Graham, J., "Definition of a Rotorcraft," `https://www.aerosociety.com/Assets/Docs/Publications/SpecialistPapers/Definition_of_a_Rotorcraft.pdf`, Februry 2013, Special paper of the Royal Aeronautical Society, available on-line.

[2] Ormiston, R. A., "Revitalising advanced rotorcraft research - and the compound helicopter ," *The Aeronautical Journal*, Vol. 120, 2016, pp. 83 – 129.

[3] Biava, M., Woodgate, M., and Barakos, G. N., "Fully implicit discrete-adjoint methods for rotorcraft applications," *AIAA Journal*, Vol. 54, No. 2, 2015, pp. 735–749.

[4] Grunwald, K. J. and Goodson, K. W., "Aerodynamic loads on an isolated shrouded-propeller configuration for angles of attack from -10 degrees to 110 degrees," Tech. rep., National Aeronautics and Space Administration Washington DC, 1962.

[5] Youngren, H., Drela, M., and Sanders, S., "Ducted Fan Design Code," `http://web.mit.edu/drela/Public/web/dfdc/`, December 2005, Ducted Fan Design Code homepage, available on-line.

[6] Drela, M. and Youngre, H., "Axisymmetric Analysis and Design of Ducted Rotors," `http://web.mit.edu/drela/Public/web/dfdc/DFDCtheory12-31.pdf`, December 2005, Ducted Fan Design Code theory, available on-line.

[7] Steijl, R., Barakos, G. N., and Badcock, K., "A framework for CFD analysis of helicopter rotors in hover and forward flight," *International Journal for Numerical Methods in Fluids*, Vol. 51, No. 8, 2006, pp. 819–847.

[8] Steijl, R. and Barakos, G. N., "Sliding mesh algorithm for CFD analysis of helicopter rotor-fuselage aerodynamics," *International Journal for Numerical Methods in Fluids*, Vol. 58, No. 5, 2008, pp. 527–549.

[9] Osher, S. and Chakravarthy, S., "Upwind schemes and boundary conditions with applications to Euler equations in general geometries," *Journal of Computational Physics*, Vol. 50, No. 3, 1983, pp. 447–481.

[10] van Leer, B., "Towards the ultimate conservative difference scheme. V. A second-order sequel to Godunov's Method," *Journal of Computational Physics*, Vol. 32, No. 1, 1979, pp. 101–136.

[11] van Albada, G. D., van Leer, B., and Roberts, W. W., "A Comparative Study of COmputational Methods in Cosmic Gas Dynamics," *Astronomy and Astrophysics*, Vol. 108, No. 1, 1982, pp. 76–84.

[12] Axelsson, O., *Iterative Solution Methods*, Cambridge University Press, 1994.

[13] Menter, F., "Two-Equation Eddy-Viscosity Turbulence Models for Engineering Applications," *AIAA Journal*, Vol. 32, No. 8, 1993, pp. 1598–1605.

[14] Chirico, G., Szubert, D., Vigevano, L., and Barakos, G. N., "Numerical modelling of the aerodynamic interference between helicopter and ground obstacles," *CEAS Aeronautical Journal*, Vol. 8, No. 4, 2017, pp. 589–611.

[15] Drela, M. and Youngren, H., "XROTOR user guide," `http://web.mit.edu/drela/Public/web/xrotor/`, 2003, auailable on-line.

9 TABLES AND FIGURES

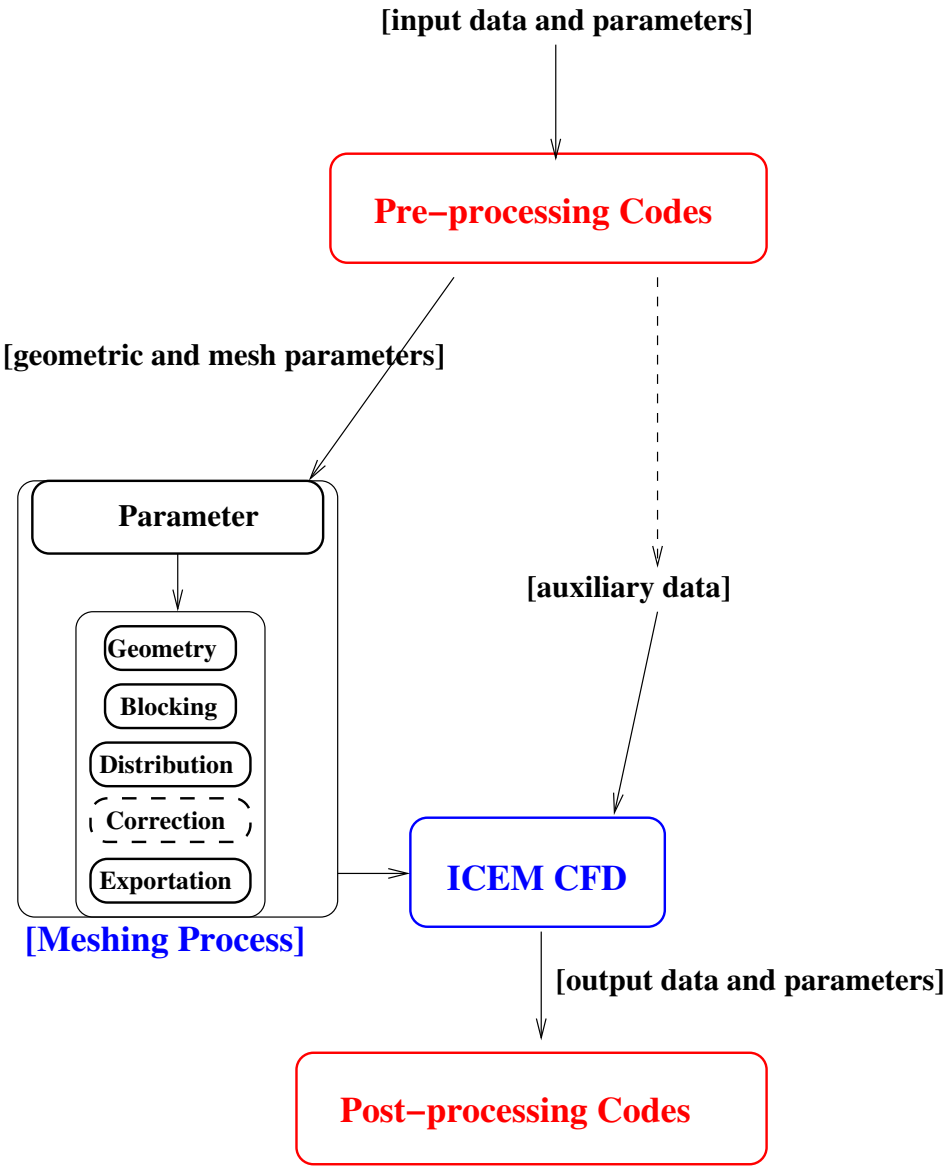

Figure 1: Flow-chart of the automation framework

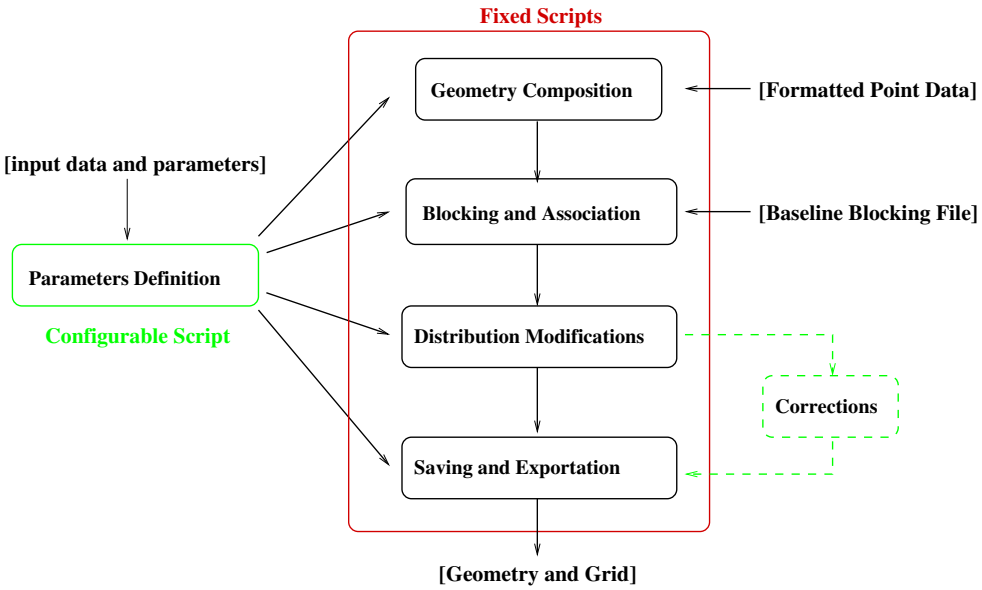

Figure 2: ICEM script modules

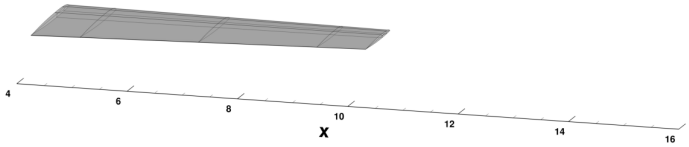

(a) Short tapered blade without twist/swept/anhedral.

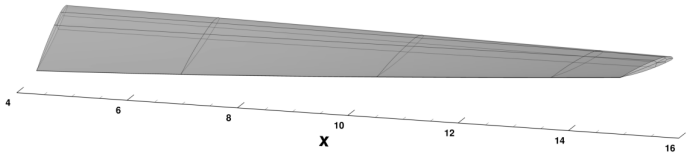

(b) Long tapered blade with a linear twist of $60°$.

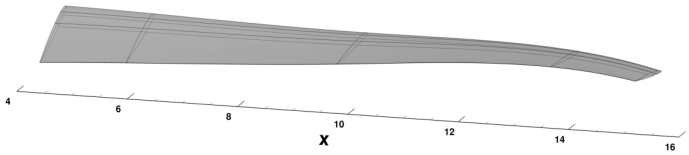

(c) Long tapered blade with a linear twist of $60°$, and a slightly swept and anhedral tip.

Figure 3: Different blade shapes

Table 1: Test conditions for the ducted fan case

Case	Configuration	Prop/Centre-body/Duct	$V_\infty[ft/s]$	AoA	RPM	μ	$\theta_{0.7}[°]$	Re	Tip/Root Clearance[inch]
Case 1	Empty duct	off/on/on	100.00	0-30	-	-	-	5.5×10^5	-
Case 2	Open propeller	on/on/off	100.00	0	8000	0.189	29.58	5.5×10^5	-/0.10
Case 3	Ducted fan	on/on/on	100.00	0	8000	0.189	29.58	5.5×10^5	0.04/0.10

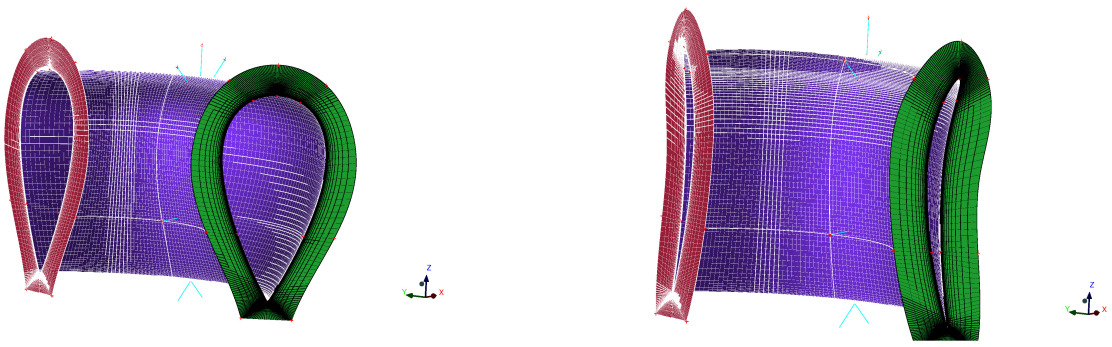

(a) Duct with NACA0050 section

(b) Duct with NACA8406 section

Figure 4: Different duct shapes using NACA0050 and NACA8406 airfoils as sections, 120° of revolution, radius= $0.727 \times c_{duct}$.

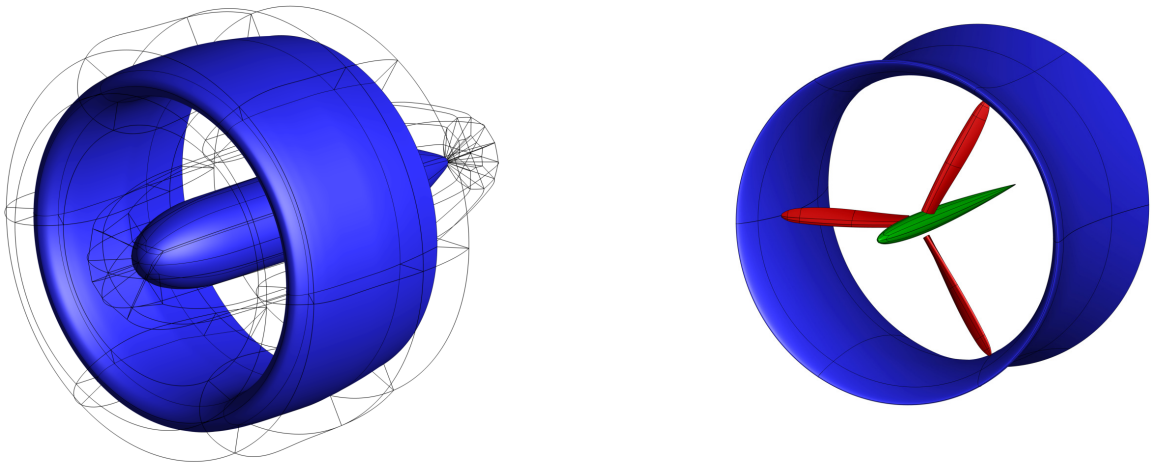

(a) Mesh topology of an empty ducted fan. The case corresponds to the experiments of Grunwald *et al.* [4]

(b) Transformed and assembled ducted fan components.

Figure 5: Assembled grid topologies and geometries

Table 2: Aerodynamic loads breakdown and comparisons between experiments, HMB3 simulations and simpler predictive methods.

C_{Fx}	EXP	Contribution	DFDC	Contribution	HMB3	Contribution	HMB3_OP	Contribution	XRotor_OP
Total	1.40	100%	1.416	100%	1.396	100%	1.355	100%	1.39
Rotor	1.00	71.4%	0.912	64.4%	0.985	70.6%	1.418	104.7%	1.39
Duct(with CB)	0.40	28.5%	0.504	35.6%	0.410	29.4%	-	-	-
Centre-body	-	-	-	-	0.068	4.9%	-0.063	-4.7%	-
Propeller C_{Mx}	0.27	-	0.391	-	0.279	-	0.313	-	0.391
Efficiency η	0.713	-	0.498	-	0.687	-	0.594	-	0.489

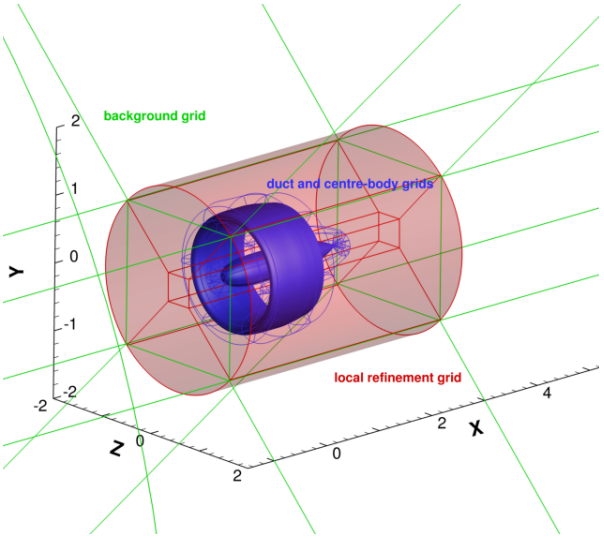

(a) Empty duct case, the duct and centre-body boundary layer grids are embedded in background grids with local refinement.

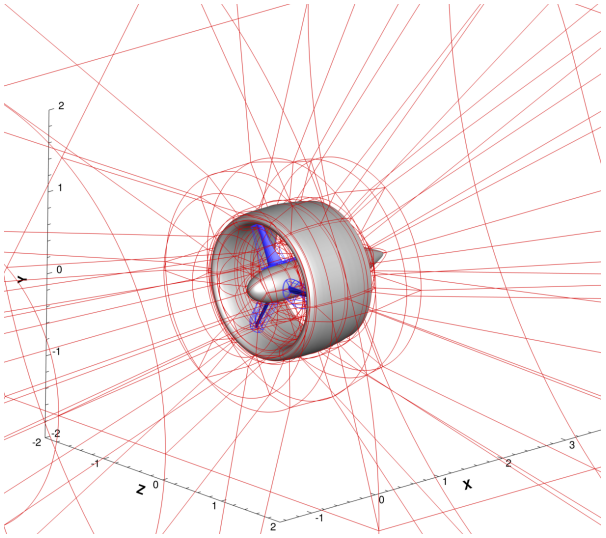

(b) Complete ducted fan case, the blade grids are embedded with the background grid, which contains the duct and centre-body.

Figure 6: Geometries, grid topology, and the coordinate system of the empty and the complete ducted fan configurations.

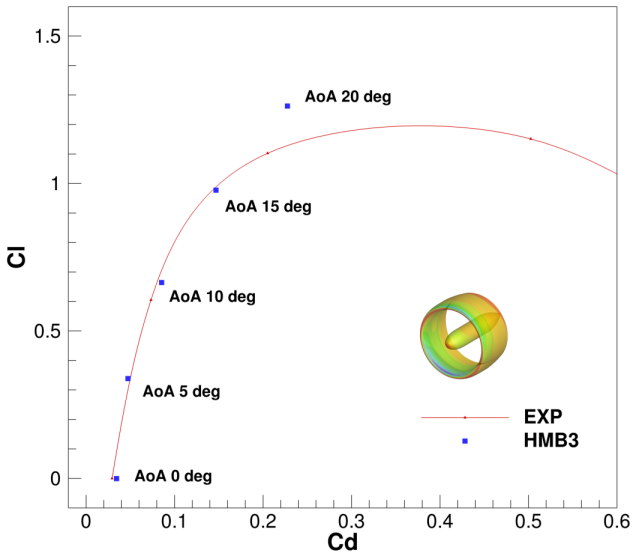

Figure 7: Drag polar comparisons for the empty duct simulations (case 1 of Table 1).

Table 3: Relative error analysis of DFDC and HMB3 predictions ($ERROR = \frac{[Prediction]-[EXP]}{[EXP]}$)

C_{Fx}	EXP	DFDC	ERROR	HMB3	ERROR
Total	1.40	1.416	1.14%	1.396	-0.32%
Rotor	1.00	0.912	-8.80%	0.985	-1.47%
Duct(with CB)	0.40	0.504	26.00%	0.410	2.56%
Centre-body	-	-	-	0.068	-
Propeller C_{Mx}	0.27	0.391	44.81%	0.279	3.35%

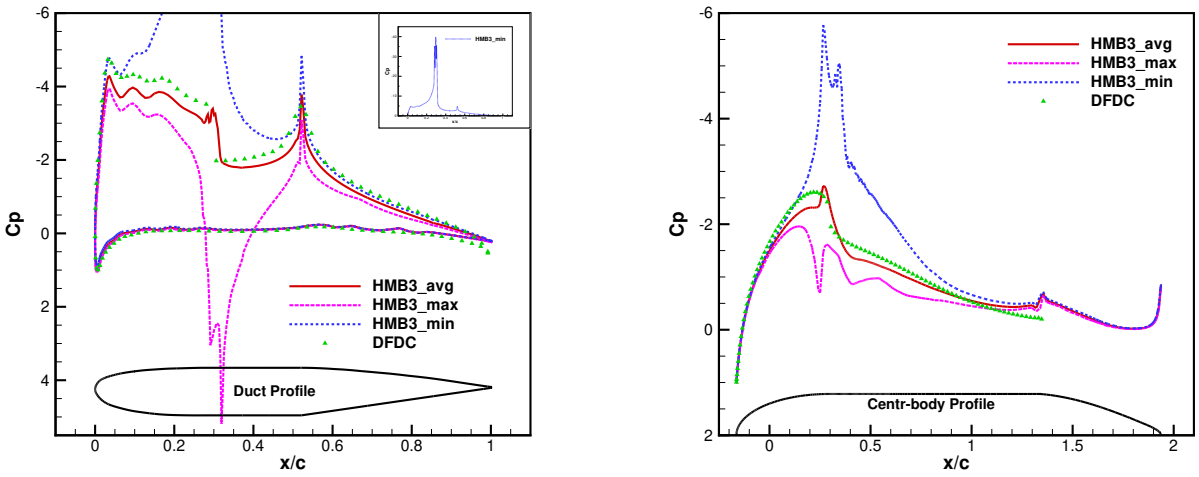

(a) Cp distribution on the duct

(b) Cp distribution on the center-body

Figure 8: Pressure coefficient distributions along the duct and center-body surface. The peak and averaged values predicted by HMB3 are compared with the method of M. Drela[5][6].

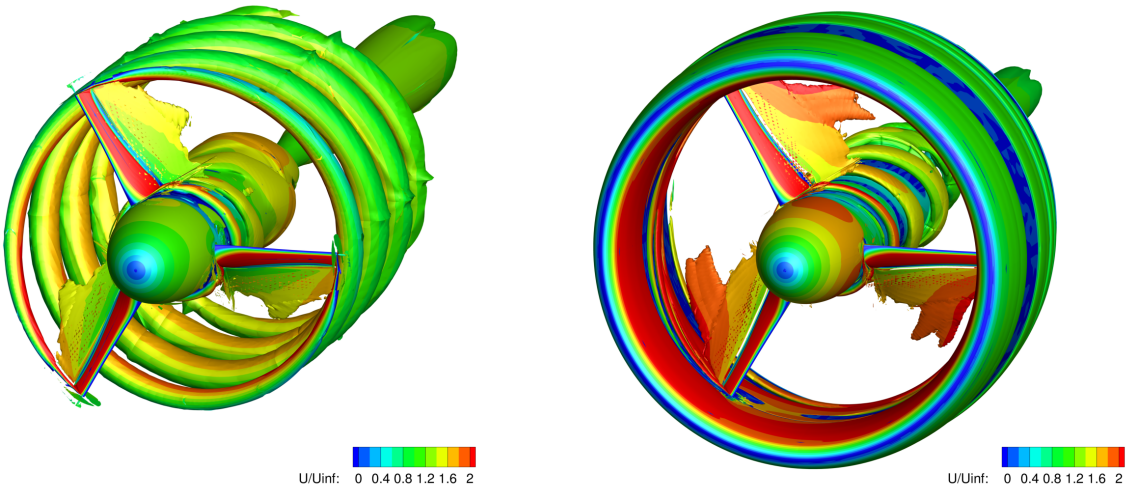

(a) Open propeller

(b) Ducted propeller

Figure 9: Iso-surfaces of non-dimensional Q=5, colored with non-dimensional axial speed, cases 2 and 3 of Table 1.

Table 4: Axial mass and momentum flow rates measured in HMB3 simulations for all cases of Table 1, integrated over the diffuser exit section (see Figures 10(a) and 10(b)).

Case	Configuration	Axial mass flow rate $\dot{m}$	Axial momentum flow rate $\dot{m}u$
Case 1	Empty duct	0.968	0.991
Case 2	Open propeller	1.363	1.946
Case 3	Ducted fan	1.439	2.139

Table 5: Axial moments breakdown for the ducted fan and the open propeller.

C_{Mx}	HMB3$_{df}$	Contribution	HMB3$_{op}$	Contribution
Total	0.282	100%	0.314	100%
Rotor	0.279	99.07%	0.313	99.8%
Duct	0.0027	0.96%	-	-

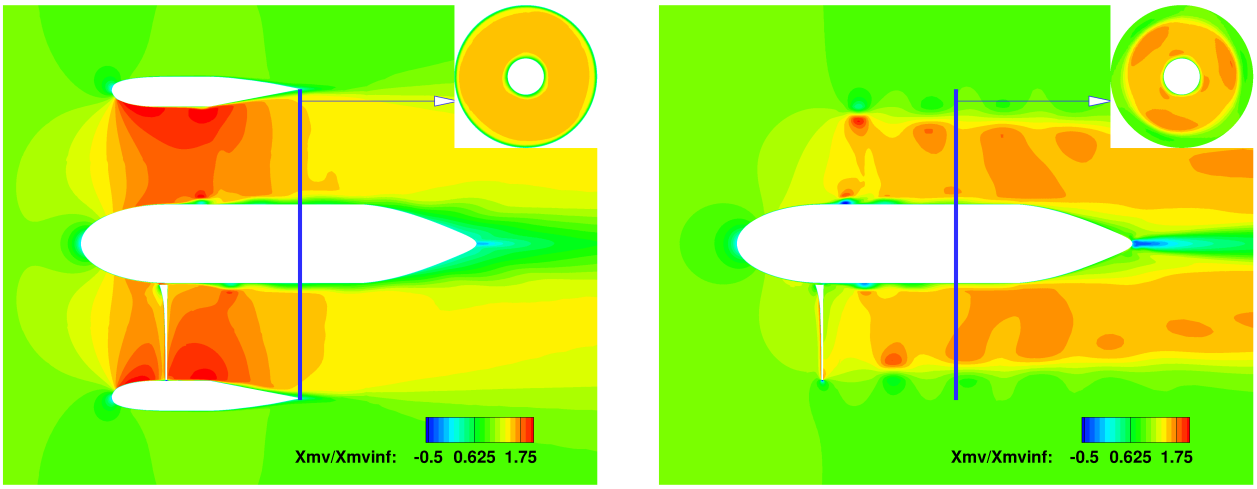

(a) Ducted propeller axial momentum

(b) Open propeller axial momentum

Figure 10: Axial momentum (normalised by the far-field axial momentum) comparisons between the ducted propeller and the open propeller (cases 2 and 3 of Table 1). Thick blue lines denote the diffuser exit sections.

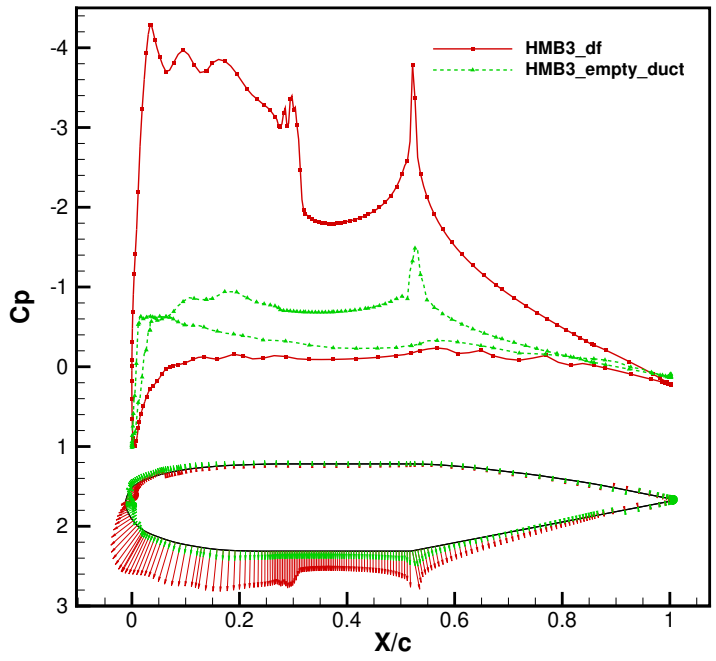

Figure 11: Static pressure coefficient distribution and pressure force vectors on the duct, with and without the propeller (cases 1 and 2 of Table 1).

Table 6: Compound rotorcraft test conditions using blade representations of steady/unsteady actuator disks and resolved blades.

Case	Main rotor model	Propeller models	$\theta_s[^\circ]$	μ
stAD	steady actuator disk	steady actuator disk	5	0.125
unsAD	unsteady actuator disk	unsteady actuator disk	5	0.125
resBld	resolved blades	unsteady actuator disk	0	0.125

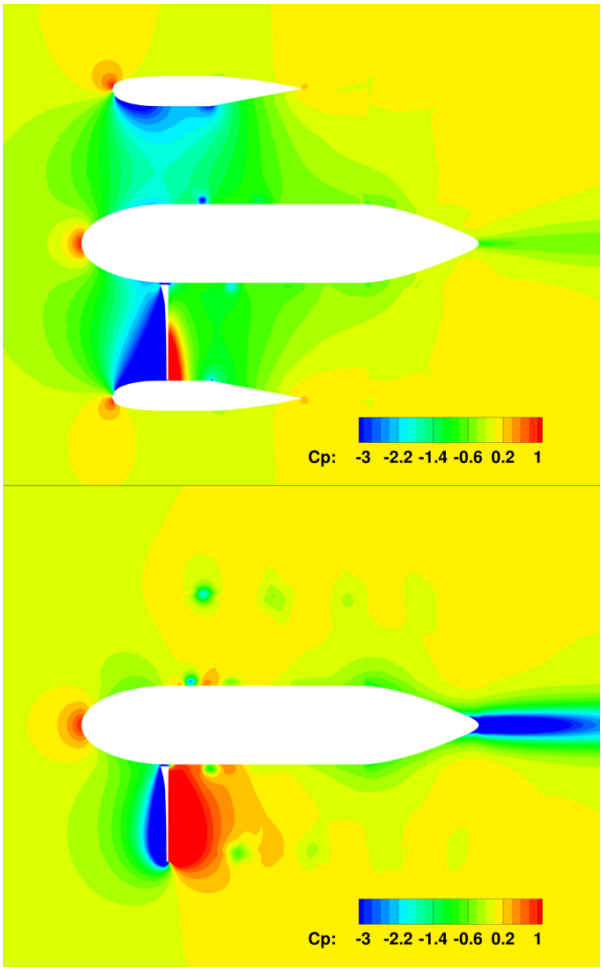

(a) Static pressure coefficient Cp comparisons

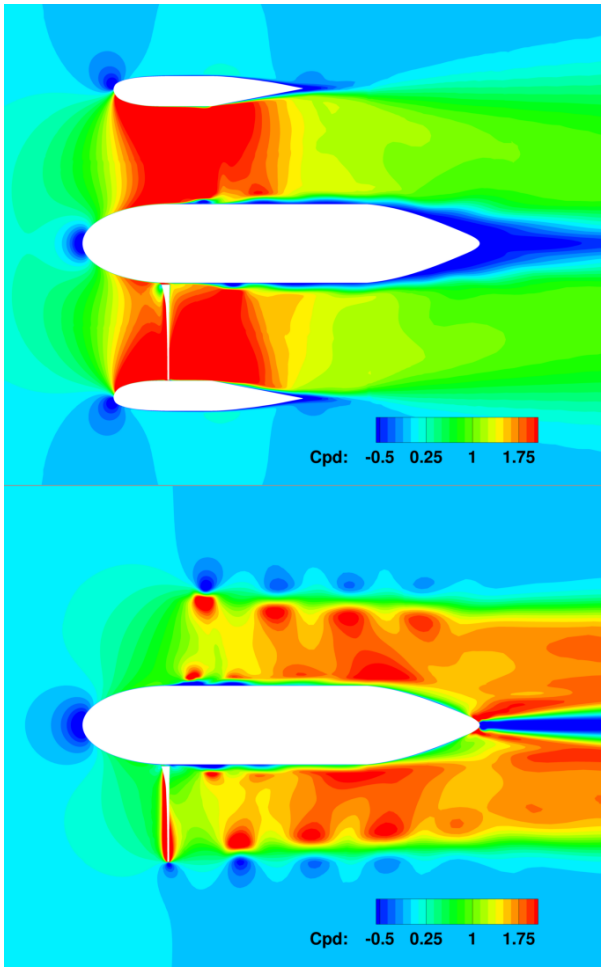

(b) Dynamic pressure coefficient Cpd comparisons($Cpd = \frac{0.5\rho V^2 - 0.5\rho_\infty V_\infty^2}{0.5\rho_\infty V_\infty^2}$)

Figure 12: Static and dynamic pressure coefficients of the ducted propeller and open propeller (cases 2 and 3 of Table 1).

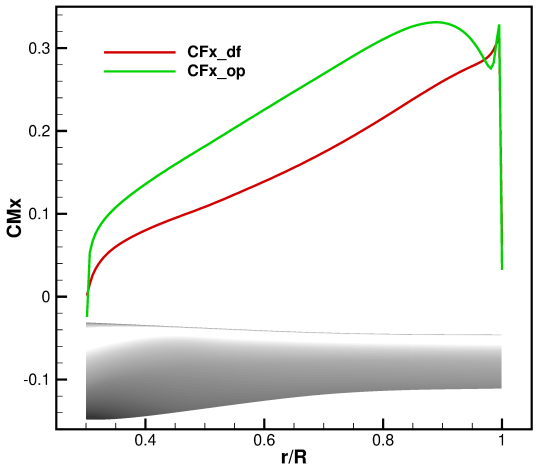

(a) Axial force distribution along the blade span

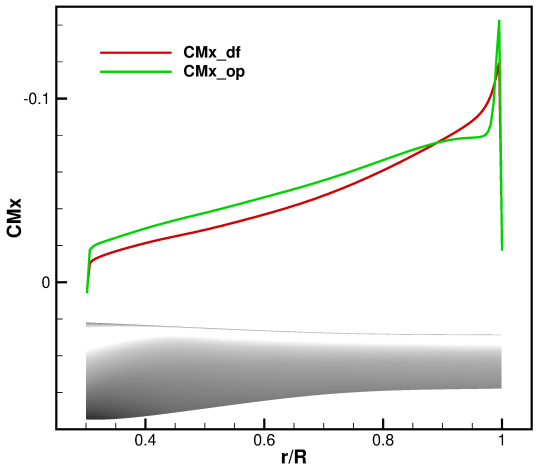

(b) Axial moment distribution along the blade span

Figure 13: Blade loads distribution along the radial direction, corresponding to cases 2 and 3 of Table 1.

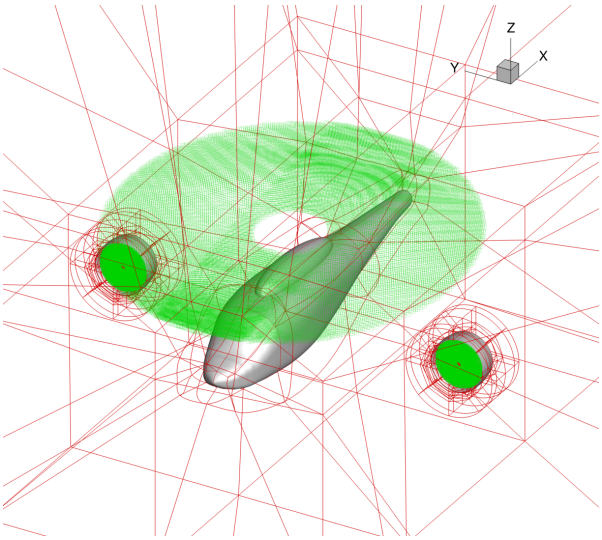

(a) Grid topology using steady nonuniform actuator disks.

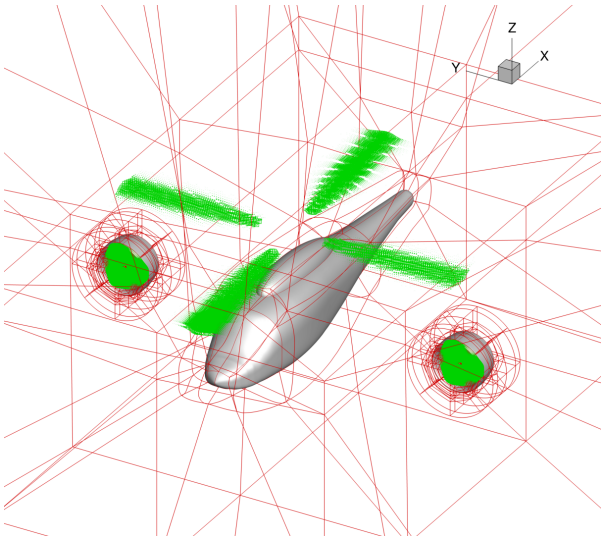

(b) Grid topology using unsteady actuator lines.

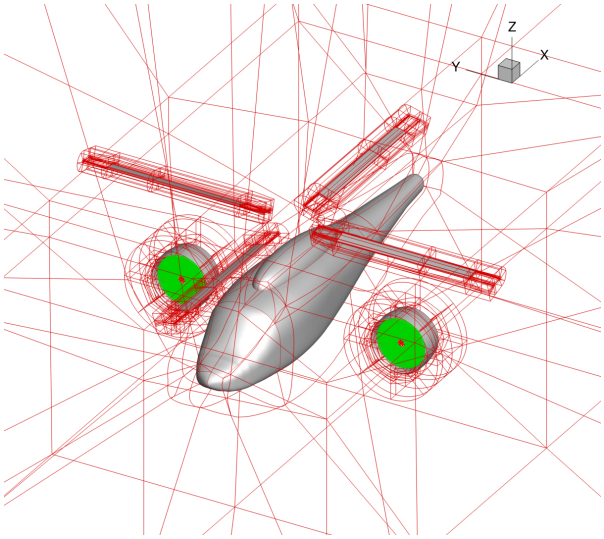

(c) Grid topology using resolved blades.

Figure 14: Multi-block mesh topologies with different blade representations.

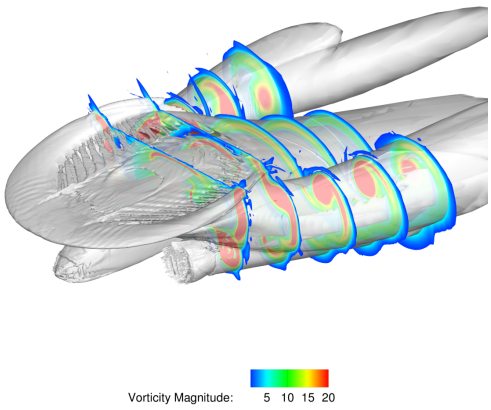

(a) Wake structure resolved using steady actuator disk.

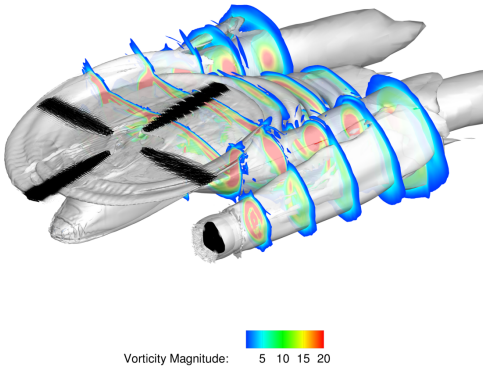

(b) Wake structure resolved using unsteady actuator lines.

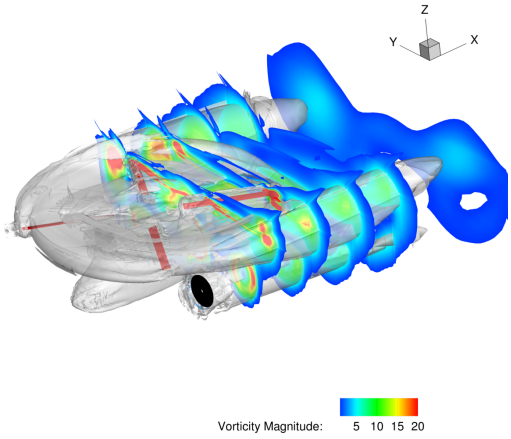

(c) Wake structure resolved using resolved blades (coarse grids).

Figure 15: Wake resolved using steady actuator disks, unsteady actuator lines, and resolved blades

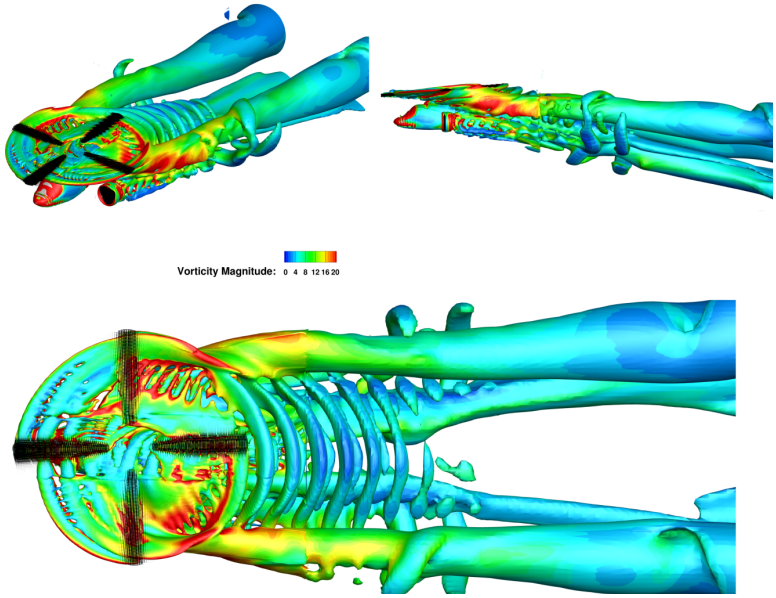

Figure 16: Wake structure obtained from unsteady actuator lines (case unsAD of Table 6) using refined wake grids (iso-surface of non-dimensional Q=0.5, colored by non-dimensional vorticity).

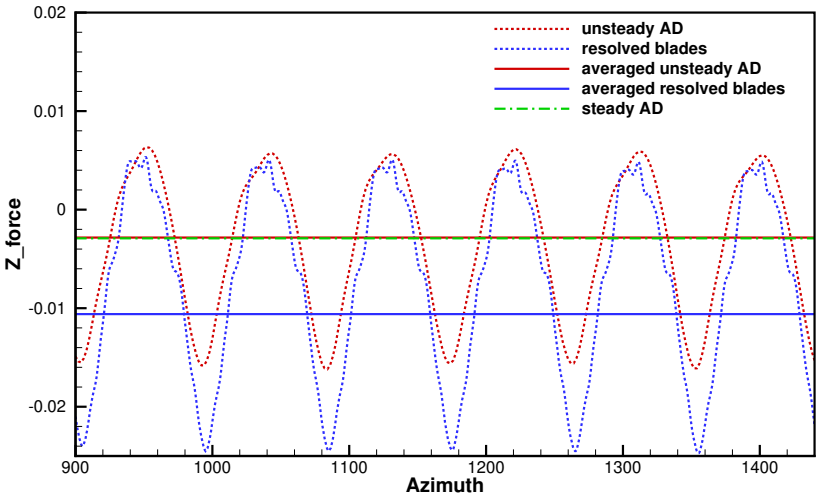

Figure 17: Lifting force on the fuselage obtained from steady actuator disks, unsteady actuator lines, and resolved blades.

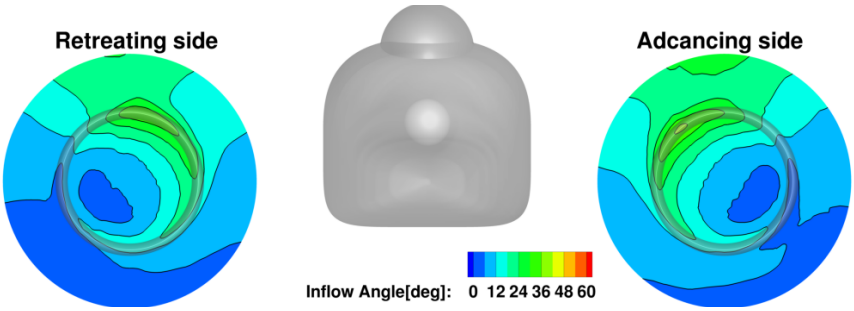

(a) Ducted fan inflow angles using steady actuator disks.

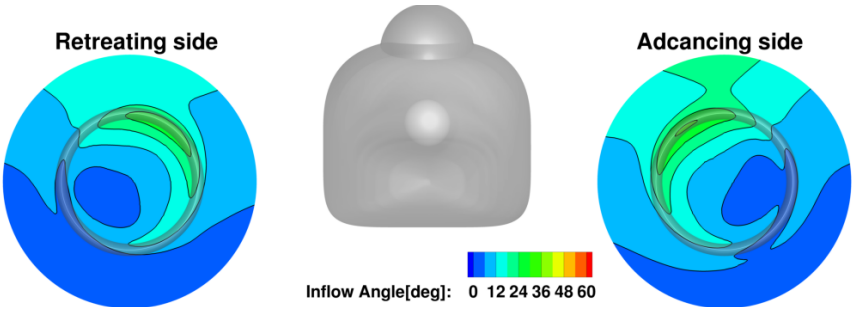

(b) Ducted fan inflow angles using unsteady actuator lines.

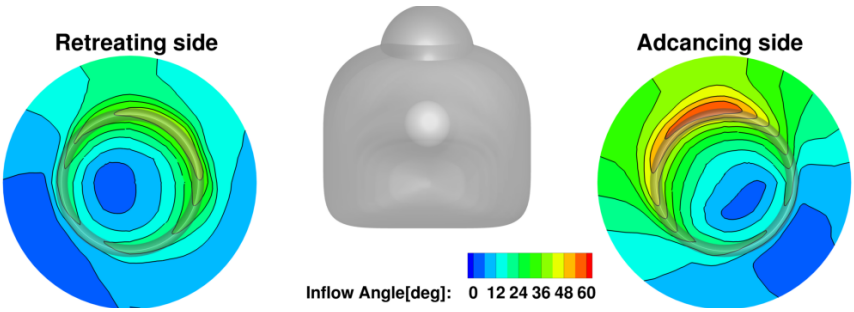

(c) Ducted fan inflow angles using resolved blades.

Figure 18: Inflow angles, measured as $\mathbf{acos}(\frac{u}{\sqrt{u^2+v^2+w^2}})$, 0.125 c_{df} ahead the ducted fan inlet for all cases of Table 6, viewed from behind the fuselage.